remote sensing

MDPI

Article

A New Method for Extracting Three-Dimensional Surface Deformation in Underground Mining Areas Based on the Differentiability of D-InSAR Line-of-Sight Displacements

Junjie Chen [1], Chunsu Zhao [1], Weitao Yan [1,2,*] and Zhiyu Chen [1]

[1] School of Surveying and Land Information Engineering, Henan Polytechnic University, Jiaozuo 454003, China; chenjj@hpu.edu.cn (J.C.); 212204010039@home.hpu.edu.cn (C.Z.); 212204010034@home.hpu.edu.cn (Z.C.)
[2] State Collaborative Innovation Center of Coal Work Safety and Clean-Efficiency Utilization, Henan Polytechnic University, Jiaozuo 454003, China
* Correspondence: yanweitao@hpu.edu.cn; Tel.: +86-13693912813

Abstract: Monitoring three-dimensional (3D) deformation in underground mining areas is crucial for the prevention and control of mining-induced disasters. Differential interferometric synthetic aperture radar (D-InSAR) is limited to detecting one-dimensional (1D) deformation along the line of sight (LOS). This paper proposes a new method for extracting 3D mining-induced deformation based on the differentiability of D-InSAR LOS deformation fields. The method approximates the D-InSAR LOS deformation field in underground mining areas as a differentiable function and constructs a 3D deformation extraction model utilizing directional derivatives of this function. The least squares method is used for estimating and evaluating the 3D deformation. Simulation and real data experiments have been used to verify the feasibility of the method in extracting mining-induced 3D deformation. The simulation results show relative root mean square errors (RRMSES) of 1.24%, 6.05%, 0.97%, and 11.47% for vertical and horizontal displacements along the east–west and south–north directions, respectively. The real data experiments using Sentinel-1 images show that the root mean square errors (RMSES) of the up–down, south–north, and east–west directions are 14.06 mm, 7.37 mm, and 11.56 mm, respectively. Experimental results show that the method can provide a certain basis for 3D surface deformation monitoring of mining subsidence.

Keywords: mining subsidence; InSAR; single-track; line-of-sight displacements; three-dimensional deformation

check for updates

Citation: Chen, J.; Zhao, C.; Yan, W.; Chen, Z. A New Method for Extracting Three-Dimensional Surface Deformation in Underground Mining Areas Based on the Differentiability of D-InSAR Line-of-Sight Displacements. *Remote Sens.* **2024**, *16*, 4085. https://doi.org/10.3390/rs16214085

Academic Editor: João Catalão Fernandes

Received: 18 September 2024
Revised: 26 October 2024
Accepted: 31 October 2024
Published: 1 November 2024

Copyright: © 2024 by the authors. Licensee MDPI, Basel, Switzerland. This article is an open access article distributed under the terms and conditions of the Creative Commons Attribution (CC BY) license (https://creativecommons.org/licenses/by/4.0/).

1. Introduction

Coal is the primary energy source in China, and its production continues to grow steadily. According to the National Bureau of Statistics of China, industrial coal production reached a record high of 4.66 billion tons in 2023, representing a 2.9% increase from the previous year. Underground coal mining, the primary method for extracting coal, creates goafs, which lead to the destruction of overlying rock and subsequent surface subsidence. This subsidence can cause various disasters, including sinkhole [1,2], building damage [3,4], surface fissures [5,6], traffic facility destruction [7], and farmland damage [8], significantly impacting public safety.

Monitoring 3D surface displacement due to mining is crucial for disaster prevention and control. Understanding surface movements induced by underground mining helps develop effective mitigation measures. At present, monitoring methods are primarily divided into point measurement and surface measurement. Point measurement techniques primarily include precise leveling, total station surveys, and Global Navigation Satellite System (GNSS) measurement [9]. These methods measure data at discrete points, typically located in characteristic points of surface subsidence basins. Although point measurement methods can provide precise discrete point information, their small coverage area and low

spatial resolution can only somewhat reflect surface movement laws. In contrast, surface measurement techniques allow for more comprehensive monitoring of surface movement by acquiring more measurement data above the mining face. Currently, surface measurement techniques primarily include photogrammetry [10,11], LiDAR scanners [12–15], and D-InSAR [16]. Photogrammetry can generate 3D coordinate information of the surface. However, the accuracy of photogrammetry is limited when the point cloud contains significant vegetation and lacks control points [17]. Additionally, photogrammetry is not sensitive enough to small deformations [11]. LiDAR scanners techniques typically calculate vertical or horizontal displacements by differencing two images generated from interpolating point clouds. This method can introduce errors in complex terrains. Furthermore, the reliability of surface deformation in such environments is affected by uncertainty factors like point density, surface roughness, and registration errors [13].

The differential interferometry synthetic aperture radar (D-InSAR) technique has been widely used in mining-subsidence monitoring due to its high accuracy, short monitoring period, and surface measurement capability [16]. However, the D-InSAR technique is susceptible to factors such as temporal decorrelation and baseline decorrelation. To overcome these shortcomings, multi-temporal InSAR (MT-InSAR) techniques are used, including the persistent scatterer InSAR technique [18] and small baseline subsets (SBAS) InSAR techniques [19]. These techniques are now widely used in mining-subsidence monitoring [20]. However, InSAR measurements provide 1D deformation along the radar LOS direction, and when the radar incidence angle is small, they are more sensitive to vertical displacement. This limitation makes it difficult to meet the requirements of 3D deformation monitoring in mining areas.

In order to extract the 3D surface displacement in the mining area from the InSAR 1D LOS deformation, many scholars have conducted studies [16,21,22]. At present, the research in this field can be classified into three primary methods according to the different data sources used: (1) The multitrack InSAR and multitrack InSAR + MAI (multiple aperture InSAR)/OT (offset tracking) method [23–26]. This method establishes a functional model based on the geometric relationship between InSAR observations and 3D surface deformation, solving for the latter via the least squares method, with the number of InSAR observations equal to or exceeding the number of unknowns (3D surface deformation). (2) The InSAR + prediction model method [27–31]. This method uses single-track InSAR measurements to invert the prediction parameters of the deformation prediction model and subsequently uses the inverted prediction parameters and the prediction model to estimate the 3D surface deformation. (3) The InSAR + prior deformation model method [22,32–36]. This method also relies on single-track InSAR measurements but utilizes a specific prior deformation model based on the mining-subsidence law to reduce the number of unknowns and construct a model for extracting 3D deformation from the 1D LOS deformation.

The first method has stringent SAR data requirements. It requires multitrack or multisource data in the study area, which is not feasible in most areas. The key to the second method lies in using optimization algorithms to estimate prediction parameters, but it cannot guarantee that the obtained parameters are globally optimal, as they may be influenced by local optima. The accuracy of 3D deformation depends on these prediction parameters, so improving their accuracy is crucial. Additionally, to implement the method, it is necessary to obtain information about the relevant parameters of the goaf, which can present additional challenges and complexities. The third method is less complex in terms of SAR data acquisition and deformation extraction compared to the previous two methods. It is suitable for extracting 3D deformation in a specific deformation region. However, the third method primarily focuses on utilizing the projection relationship between 3D surface deformation and LOS deformation to construct a model for extracting 3D deformation. Moreover, few studies have focused on the characteristics of the LOS deformation field induced by underground mining and the use of these characteristics to construct a 3D deformation extraction model.

Therefore, this paper proposes a new model for extracting 3D mining-induced deformation based on single-track D-InSAR deformation characteristics. First, the D-InSAR LOS deformation field in the underground mining area can be approximated as a differentiable function. By exploiting the existence of all directional derivatives of the differentiable function, a 3D deformation extraction model is constructed. Then, the least squares method is used to estimate 3D deformation and evaluate its uncertainty.

2. Methodology

2.1. Differentiability of the LOS Deformation Fields of the Underground Mining Area

The 1D displacements $LOS(x, y)$ along the LOS direction based on D-InSAR technique is a composite of the vertical, south–north, and east–west displacement components (see Figure 1), which can be expressed as follows [37]:

$$LOS(x, y) = C_1 W(x, y) + C_2 U_N(x, y) + C_3 U_E(x, y) \tag{1}$$

where $C_1 = \cos\theta_0$; $C_2 = -\sin\theta_0 \cos(\alpha_h - 3\pi/2)$; $C_3 = -\sin\theta_0 \sin(\alpha_h - 3\pi/2)$; α_h is the azimuth of the satellite flight direction; $W(x, y)$, $U_N(x, y)$, and $U_E(x, y)$ are the vertical, south–north, and east–west displacements, respectively; θ_0 is the incidence angle of the satellite. The incidence angle θ_0 varies at each pixel in a SAR image, but for a small study area, this variation is negligible. Therefore, this paper averages the incidence angles and treats $LOS(x, y)$ as a binary function.

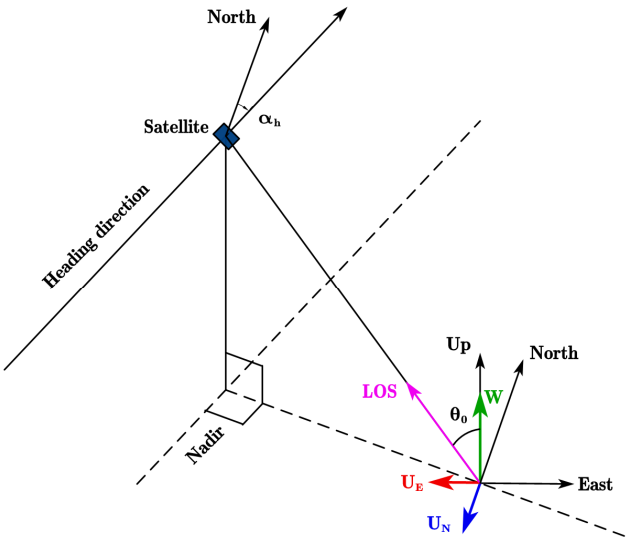


Figure 1. Relationship between surface 3D deformation and LOS direction deformation.

The surface movement vector due to underground mining points to the center of the surface displacement basin. The surface movement vectors are directional. As shown in Figure 1, the surface movement vectors that point up, south, and west are defined as positive. According to the probability integration method (PIM) prediction model, $U_N(x, y)$ and $U_E(x, y)$, in the case of inclined coal seam mining, can be expressed as follows [33,38]:

$$U_N(x, y) = b \cdot r \cdot \frac{\partial W(x, y)}{\partial x} + W(x, y) \cot\theta \cos\varphi \tag{2}$$

$$U_E(x, y) = b \cdot r \cdot \frac{\partial W(x, y)}{\partial y} + W(x, y) \cot\theta \sin\varphi \tag{3}$$

In Equations (2) and (3), b is the horizontal displacement factor; r represents the radius of major mining influence and $r = H/\tan\beta$; H and β are mining depth and the major influence angle; θ is the angle of maximum subsidence, and when $\theta = 90°$, it corresponds to the case of horizontal coal seam mining; $W(x, y) \cot\theta$ is the sliding parameter in the dip

direction due to the inclination of the coal seam; φ is the angle between the dip direction and the south–north direction (dip azimuth in Figure 2). In Figure 2, $x'o'y'$, $x'oy'$, and xoy are the coordinate system of the working face, the coordinate system of the ground surface, and the geodetic coordinate system, respectively; α is the coal seam dip angle; P is the vertical plane passing through the point (x, y) and parallel to the dip.

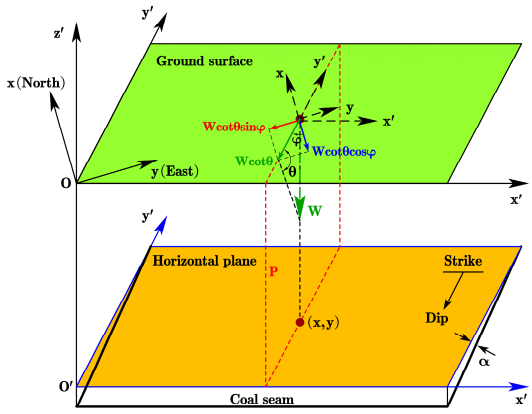


Figure 2. Decomposition of the sliding parameter $W(x, y)\cot\theta$ along the south–north and east–west directions.

Substituting Equations (2) and (3) into Equation (1), we can obtain the following:

$$LOS(x, y) = A_1 W(x, y) + A_2 \frac{\partial W(x, y)}{\partial x} + A_3 \frac{\partial W(x, y)}{\partial y} \tag{4}$$

where $A_1 = C_1 + C_2 \cdot \cot\theta \cos\varphi + C_3 \cdot \cot\theta \sin\varphi$; $A_2 = C_2 \cdot b \cdot r$; $A_3 = C_3 \cdot b \cdot r$.

According to the PIM prediction model, the surface subsidence $W(x, y)$ caused by coal seam extraction in underground mining areas, along with its first-order derivatives $\frac{\partial W(x,y)}{\partial x}$ and $\frac{\partial W(x,y)}{\partial y}$ (i.e., surface tilt), are differentiable functions. Consequently, the $LOS(x, y)$ in Equation (4) is also a differentiable function. Since the $LOS(x, y)$ in underground mining areas is differentiable, the directional derivative of the function along any direction $v = (\cos\varphi_D, \sin\varphi_D)$ exists. And the directional derivatives can be expressed by the following two equations, respectively:

$$D_v LOS(x, y) = \lim_{t\to 0} \frac{LOS(x + t\cos\varphi_D, y + t\sin\varphi_D) - LOS(x, y)}{t} \tag{5}$$

$$D_v LOS(x, y) = \frac{\partial LOS(x, y)}{\partial x}\cos\varphi_D + \frac{\partial LOS(x, y)}{\partial y}\sin\varphi_D \tag{6}$$

2.2. Three-Dimensional Mining-Induced Surface Deformation Extracting Method by Using Single-Track D-InSAR

2.2.1. Finite Difference Method for Calculating the Rate of Change in LOS Deformation Fields

Before modeling, the continuity of LOS deformation field must be ensured. However, if InSAR decoherence exists, there will be missing values in the LOS deformation field obtained by D-InSAR, which destroys the continuity of LOS deformation field. At this time, Kriging interpolation is used to fill in missing data in the LOS deformation field caused by InSAR coherence loss. This allows for the extraction of 3D deformations based on continuous LOS deformation field. The influence of interpolation is considered limited and local [32,36]. It is important to note that when the coherence of the study area is good, meaning there are no missing values in the LOS deformation field, the interpolation step is not required.

After geocoding, the LOS deformation fields are defined at the grid point (i, j), as shown in Figure 3, where $i = 1, 2, \ldots m$, $j = 1, 2, \ldots, n$. Let $f = LOS(x, y)$. According to Equation (5), for point (i, j), the directional derivatives of $LOS(x, y)$ in the eight directions with $\varphi_D = [0, \pi/4, \pi/2, 3\pi/4, \pi, 5\pi/4, 3\pi/2, 7\pi/4]$ can be approximated by the following:

$$D_\varphi f(i,j) \approx \frac{f(i + \Delta i_\varphi, j + \Delta j_\varphi) - f(i,j)}{d_\varphi} \tag{7}$$

where Δi_φ and Δj_φ represent the increments along direction φ, and d_φ denotes the step size. The specific parameters for the different directions are shown in Table 1.

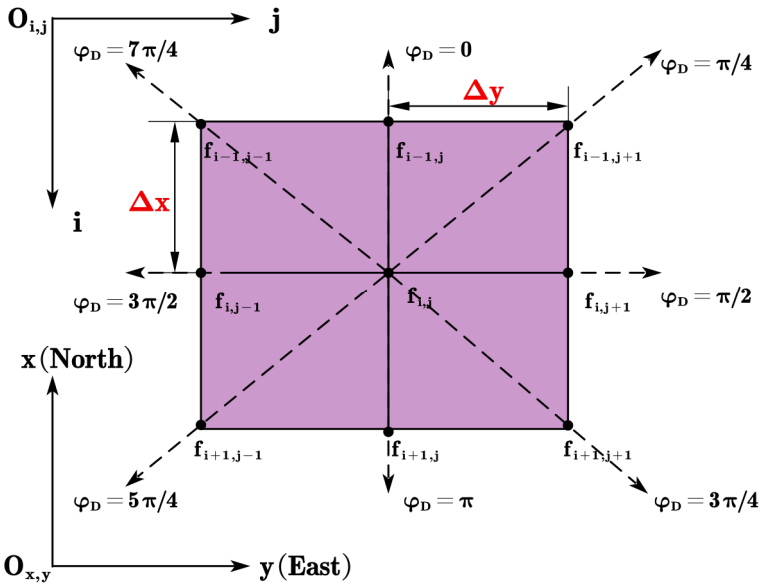


Figure 3. The arrangement of the LOS deformation raster map. Δx and Δy represent the grid resolution in the X-axis and Y-axis directions, respectively.

Table 1. Parameters of the finite difference approximation for different directions.

φ	Δi_φ	Δj_φ	d_φ
0	−1	0	Δx
$\pi/4$	−1	1	$\sqrt{(\Delta x)^2 + (\Delta y)^2}$
$\pi/2$	0	1	Δy
$3\pi/4$	1	1	$\sqrt{(\Delta x)^2 + (\Delta y)^2}$
π	1	0	Δx
$5\pi/4$	1	−1	$\sqrt{(\Delta x)^2 + (\Delta y)^2}$
$3\pi/2$	0	−1	Δy
$7\pi/4$	−1	−1	$\sqrt{(\Delta x)^2 + (\Delta y)^2}$

The second-order central difference approximation formula for the first-order partial derivatives and the second-order partial derivatives of the function f at the grid point (i, j) are the following:

$$\frac{\partial f(i,j)}{\partial x} \approx \frac{f(i-1,j) - f(i+1,j)}{2\Delta x} \tag{8}$$

$$\frac{\partial f(i,j)}{\partial y} \approx \frac{f(i,j+1) - f(i,j-1)}{2\Delta y} \tag{9}$$

$$\frac{\partial^2 f(i,j)}{\partial x^2} \approx \frac{f(i-1,j) - 2f(i,j) + f(i+1,j)}{\Delta x^2} \tag{10}$$

$$\frac{\partial^2 f(i,j)}{\partial y^2} \approx \frac{f(i,j+1) - 2f(i,j) + f(i,j-1)}{\Delta y^2} \tag{11}$$

When calculating the derivatives at the boundary grid points, a Dirichlet boundary condition is applied, assigning a value of zero to the function at the points around the boundary:

$$f(i,j) = 0 \text{ for } i = 0,\ i = m+1,\ j = 0, \text{ and } j = n+1 \tag{12}$$

Surface deformation from underground mining is primarily characterized by subsidence, which often leads to the formation of a surface subsidence basin—an area much larger than the working face. The outermost boundary of this basin is typically defined by the point where surface subsidence reaches −10 mm, as illustrated by ABCD in Figure 4, and is usually determined by the boundary angle. In Figure 4, AB and CD represent the major sections along the strike and dip of the subsidence basin, respectively. δ_0 indicates the strike boundary angle, while β_0 and γ_0 mark the down-dip and up-dip boundary angles. The area beyond this boundary is generally considered unaffected by underground mining, with deformation values assumed to be zero [38,39]. Therefore, when the extent of the LOS deformation map exceeds that of the subsidence basin, the boundary points of the map can reasonably be assumed to have zero deformation value, justifying the boundary condition defined in Equation (12).

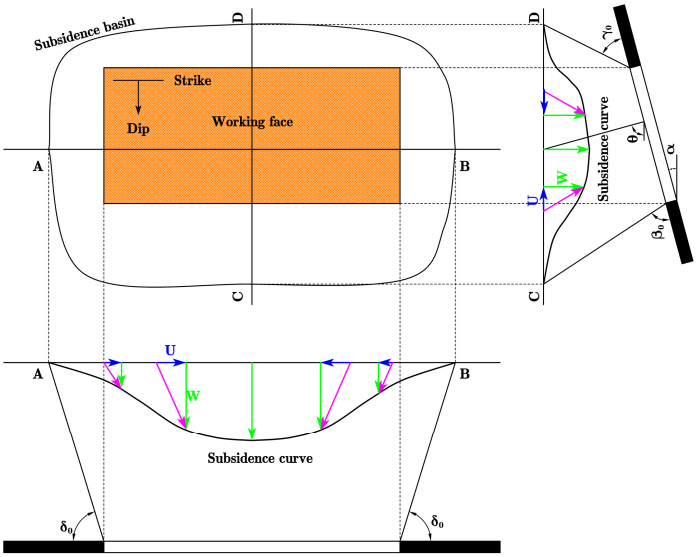


Figure 4. Determination of the boundary of the surface movement basin. AB and CD represent the major sections along the strike and dip of the subsidence basin, respectively. The green, blue and red arrows represent the subsidence vector W, the horizontal movement vector U and the vector sum of the first two, respectively.

According to Equations (7) and (12), the directional derivatives of $LOS(x,y)$ in eight directions are calculated using the finite difference method (FDM) [40]:

$$L = \begin{pmatrix} D_0 \\ D_{\pi/4} \\ D_{\pi/2} \\ D_{3\pi/4} \\ D_{\pi} \\ D_{5\pi/4} \\ D_{3\pi/2} \\ D_{7\pi/4} \end{pmatrix} LOS \tag{13}$$

where LOS is the column vector of the LOS deformation fields expanded in the order of rows, with dimensions $m \times n$ rows and 1 column; Matrices D_0, $D_{\pi/4}$, $D_{\pi/2}$, $D_{3\pi/4}$, D_{π}, $D_{5\pi/4}$, $D_{3\pi/2}$, and $D_{7\pi/4}$ are the directional derivative matrices corresponding to the eight directions, each with dimensions $m \times n$ rows and $m \times n$ columns; L represents the values of the directional derivative of $LOS(x, y)$ in the eight directions, and it has dimensions $8 \times m \times n$ rows and 1 column.

According to Equation (4), the $LOS(x, y)$ in the mining area can be expressed by $W(x, y)$ alone. Substituting Equation (4) into Equation (6), also utilizing the FDM, the directional derivatives of the $LOS(x, y)$ in the directions φ_D can be represented by $W(x, y)$ as follows:

$$L_{\varphi_D} = B_{\varphi_D} W \tag{14}$$

where

$$\begin{cases} B_{\varphi_D} = \cos\varphi_D K_1 + \sin\varphi_D K_2 \\ K_1 = C_1 \cdot D_x + (D_{xx} \cdot b \cdot r + D_x \cdot \cot\theta \cos\varphi) \cdot C_2 \\ + \left(D_x D_y \cdot b \cdot r + D_x \cdot \cot\theta \sin\varphi\right) \cdot C_3 \\ K_2 = C_1 \cdot D_y + \left(D_x D_y \cdot b \cdot r + D_y \cdot \cot\theta \cos\varphi\right) \cdot C_2 \\ + \left(D_{yy} \cdot b \cdot r + D_y \cdot \cot\theta \sin\varphi\right) \cdot C_3 \end{cases} \tag{15}$$

D_x, D_y, D_{xx}, and D_{yy} are first-order and second-order derivative matrices according to Equations (8)–(11) and boundary conditions defined in Equation (12); L_{φ_D} is the directional derivative of $LOS(x, y)$ along the φ_D direction; W is the column vector of vertical displacements.

2.2.2. Least Squares Estimation of 3D Surface Deformation

According to Equations (5) and (6), Equation (13) can be computed using Equation (14) to obtain the following:

$$L_{num,1} + \Delta_{num,1} = B_{num,t} W_{t,1} \tag{16}$$

where $B_{num,t} = [B_0, B_{\pi/4}, B_{\pi/2}, B_{3\pi/4}, B_{\pi}, B_{5\pi/4}, B_{3\pi/2}, B_{7\pi/4}]^T$; $num = 8 \times m \times n$, $t = m \times n$; $\Delta_{num,1}$ represents noise and is considered to follow a normal distribution.

In Equation (16), the vector L is known from Equation (13), but the vertical displacements W are unknown and need to be determined. The least squares solution to the system of linear Equations in Equation (16) is the following:

$$W = \left(B^T P B\right)^{-1} B^T P L \tag{17}$$

where P is the weighting matrix of L.

The observations L in Equation (17) are considered to be independent, making the weighting matrix diagonal. In calculating L, the FDM is used to approximate the derivatives with errors proportional to the squares of the variations $(\Delta x)^2$, $(\Delta y)^2$, and $\left((\Delta x)^2 + (\Delta y)^2\right)$. The observations for $(\Delta x)^2$ are treated as unit-weighted, leading to the following weights:

$$P_x = \frac{(\Delta x)^2}{(\Delta x)^2}, P_y = \frac{(\Delta x)^2}{(\Delta y)^2}, P_l = \frac{(\Delta x)^2}{(\Delta x)^2 + (\Delta y)^2} \tag{18}$$

According to Equations (2) and (3), U_N and U_E are obtained using W from Equation (17). According to least squares adjustment, the variance–covariance matrices of W, U_N, and U_E are the following:

$$D_{WW} = \hat{\sigma}_0^2 {N_{bb}}^{-1} \tag{19}$$

$$D_{NN} = \hat{\sigma}_0^2 F_1 N_{bb}^{-1} F_1^T \tag{20}$$

$$D_{EE} = \hat{\sigma}_0^2 F_2 N_{bb}^{-1} F_2^T \tag{21}$$

where $\hat{\sigma}_0$ is the unit-weighted root-mean-squared error; $N_{bb} = B^T P B$; $F_1 = b \cdot r \cdot D_x + \cot\theta \cos\varphi$; $F_2 = b \cdot r \cdot D_y + \cot\theta \sin\varphi$.

In summary, we established the extraction model for surface 3D deformation W, U_N, and U_E from the LOS deformation map and evaluated the uncertainty of the 3D deformation. The 3D deformation extraction model based on the differentiability of the LOS deformation field in underground mining area proposed in this paper is named "Differentiable LOS-Based 3D Deformation Extraction Model" and abbreviated as DLB-3DEM.

2.3. Workflow of the DLB-3DEM Method

The overall processing flow of the DLB-3DEM method is as follows (see Figure 5):

(1) Clip LOS deformation map to obtain the study area containing the entire mining-induced deformation basin, with points around the boundary assumed to have zero deformation as they are unaffected by mining.

(2) Retrieve the image resolution Δx and Δy of LOS deformation map. Obtain information about the coal-mining geological condition in the study area, including the mining depth H, the major influence angle β, the horizontal displacement b, the maximum subsidence angle θ, and the dip azimuth φ.

(3) Use the FDM to calculate the directional derivatives of the LOS deformation field in eight specified directions. Use these as observations for the deformation extraction model.

(4) Solve the system of linear observation equations using the least squares method to obtain vertical displacements W. Based on vertical displacements, calculate horizontal movements U_N and U_E. Evaluate the uncertainty of the extracted 3D deformations through least squares adjustment.

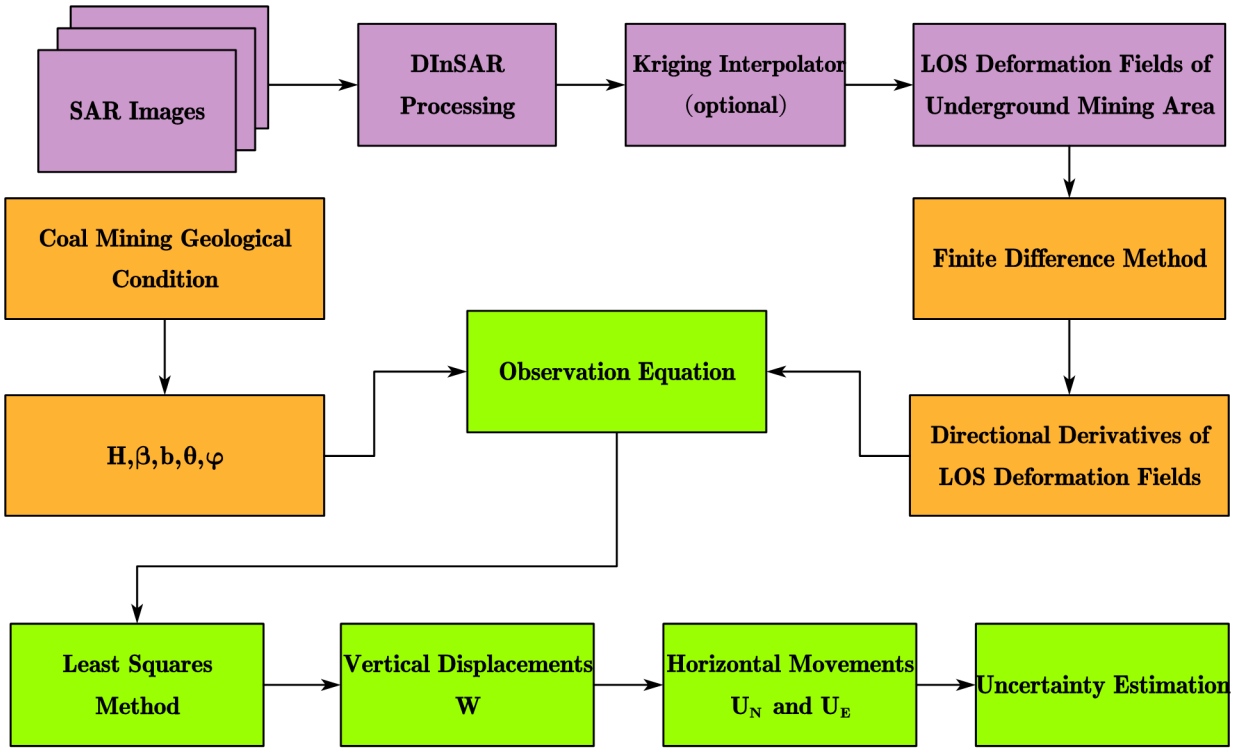


Figure 5. Flowchart of DLB-3DEM method.

3. Simulated Experiments

3.1. Experimental Data

To study the feasibility of the DLB-3DEM method proposed in this paper, we simulated an underground, inclined coal-mining working face. The parameters of the coal-mining geological condition are set as follows: coal mining thickness: M = 3 m, mining depth: H = 560 m, coal seam dip angle: 10°, dip azimuth: 180°, and a mining dimension of

$D_1 \times D_3$ = 300 m × 600 m. The mining degree coefficient along the strike and dip are, respectively, $D_3/H = 1.07 < 1.2$ and $D_1/H = 0.54 < 1.2$. The mining degree is subcritical [39]. The PIM prediction parameters are the following: subsidence coefficient q = 0.7, horizontal displacement factor b = 0.3, tangent of main influence angle tan β = 2.0, angle of maximum subsidence θ = 85°, and inflection point offset $S_1 = S_2 = S_3 = S_4 = 0$.

The parameters of the SAR data are designed as follows: the incidence angle of the satellite θ_0 = 41.843°, the azimuth of the satellite flight direction α_h = 347.019°, and the image resolution of 15 m × 15 m. The steps to simulate the LOS deformation fields induced by coal seam extraction are as follows: (a) firstly, the surface of the study area is discretized into discrete points at 15 m intervals in the south–north and east–west directions; (b) then, the vertical, south–north, and east–west displacements of these discrete points are predicted using coal-mining geological condition parameters and PIM prediction model [31] (see Figure 6a–c); (c) finally, the 3D surface deformations are projected onto the LOS direction to obtain the LOS deformation of the discrete points using Equation (1). The simulated LOS deformation is shown in Figure 6d. The simulation experiments were performed in MATLAB 7.11 software.

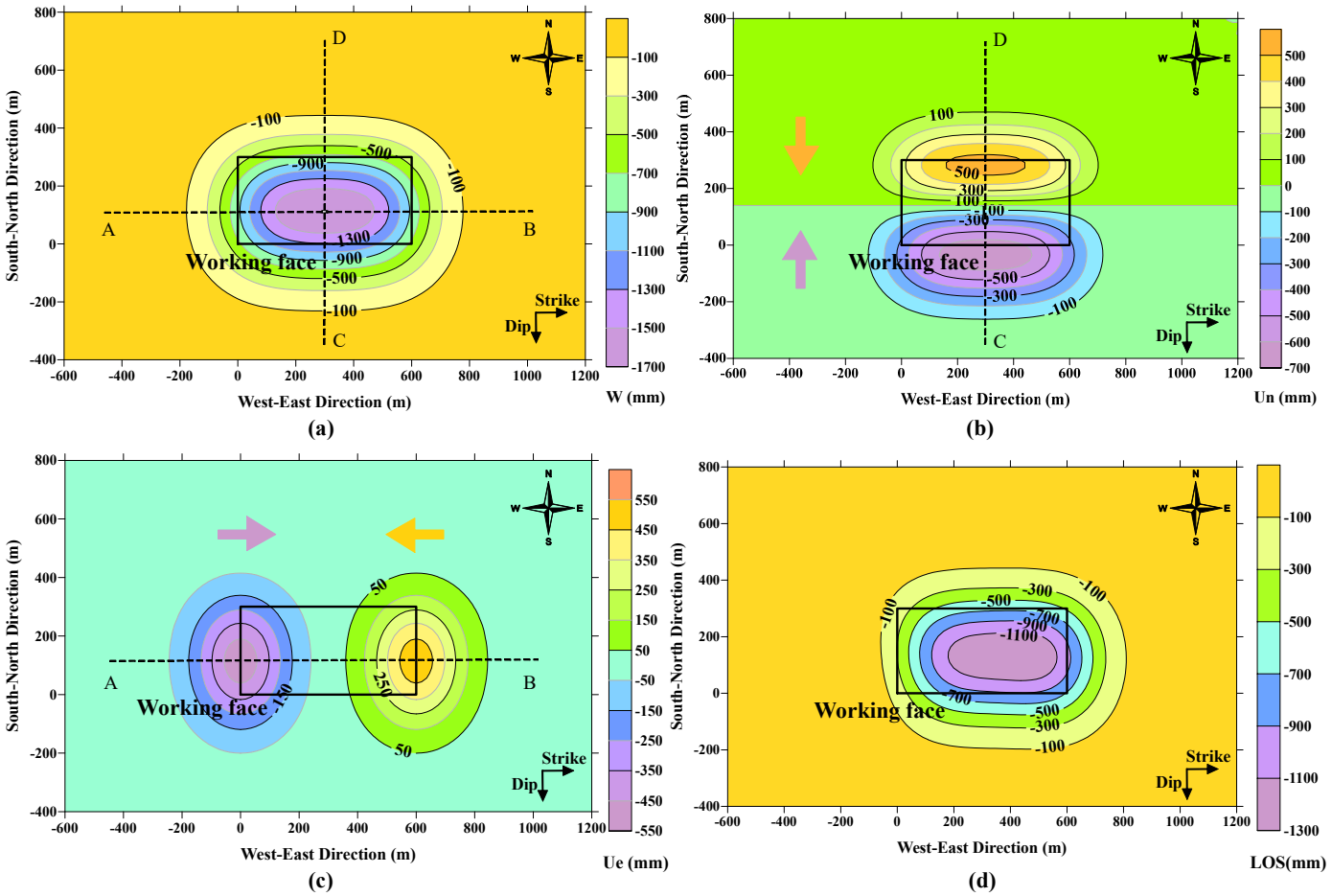


Figure 6. Simulated 3D deformation and LOS deformation value: (**a**) simulated vertical displacements value, (**b**) simulated south–north horizontal displacements value, (**c**) simulated east–west horizontal displacements value, (**d**) simulated LOS deformation value. The arrows in (**b**,**c**) represent the direction of horizontal movement. Profiles AB and CD represent survey lines within the major section of the subsidence basin.

In mining-subsidence engineering, mining-subsidence laws are determined by placing surface movement observation stations above the working face. Most stations utilize profile line observations, where the strike and dip lines intersect perpendicularly and are

positioned along the major sections of the subsidence basin's strike and dip [38]. In Figure 6, two profile lines, AB and CD, are positioned within the major section of the strike and dip of the subsidence basin, respectively.

3.2. Three-Dimensional Deformation Extraction Results and Analysis

Based on the simulated LOS deformation field of the working surface, the 3D surface deformation and its uncertainty were evaluated using the DLB-3DEM method, and the results are shown in Figure 7.

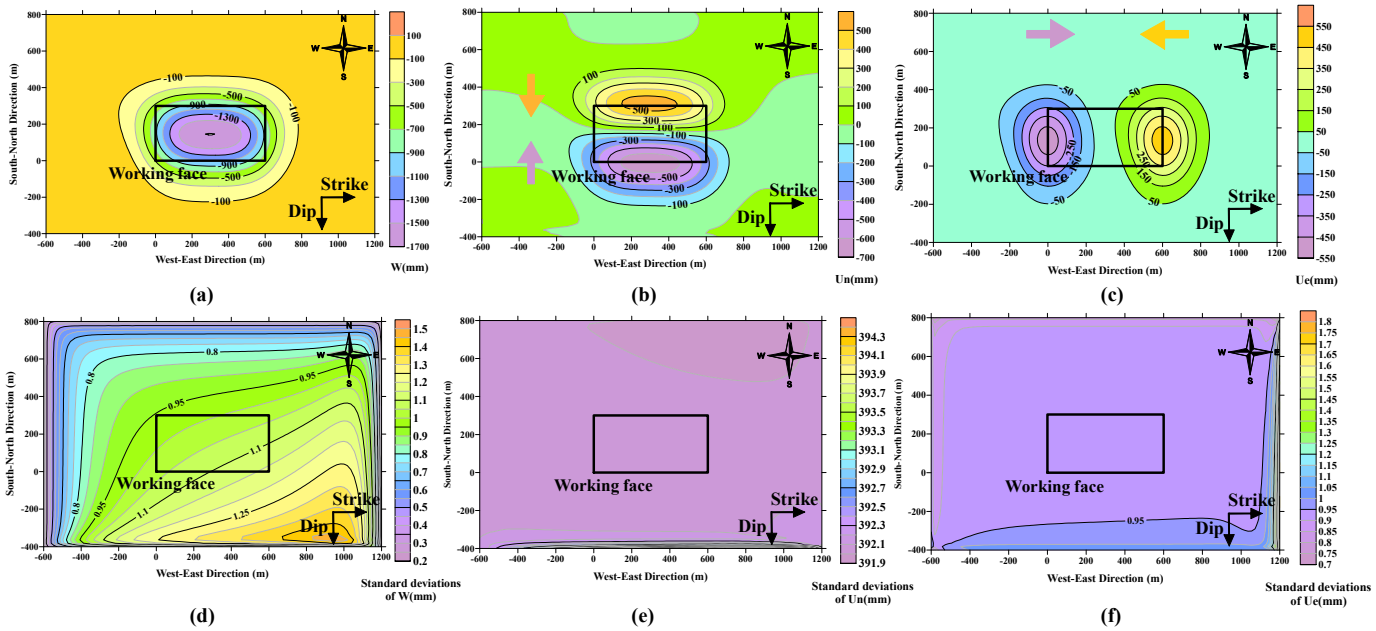


Figure 7. Three-dimensional deformation and standard deviations map extracted using the DLB-3DEM method: (**a**) extracted vertical displacements value, (**b**) extracted south–north horizontal displacements value, (**c**) extracted east–west horizontal displacements value, (**d**) standard deviations map of vertical displacements, (**e**) standard deviations map of south–north displacements, (**f**) standard deviations map of east–west displacements.

Figure 7d–f indicate that the maximum standard deviations values of the extracted vertical displacements, south–north horizontal displacements, and east–west horizontal displacements are 1.57 mm, 394.5 mm, and 1.85 mm, respectively. The reasons for the large standard deviation of the extracted deformation values in the north–south direction include the following: (1) In the current configuration of polar-orbiting SAR satellites, the LOS direction measurement of the InSAR is less sensitive to displacement in the south–north direction, where the displacement accounts for a smaller proportion of the LOS direction deformation [32,41]. (2) The larger value of the coefficient matrix F_1 in Equation (20), resulting from the dip direction of the simulated coal seam being along the south–north direction, amplifies the error in the extracted deformation.

The standard deviations of the extracted deformation values reflect their uncertainty and enable a qualitative analysis of the reliability of the extraction results. In order to verify the accuracy of the extraction results, a quantitative analysis was conducted. The deformation values along profile lines AB and CD were extracted from both the simulated 3D deformation field and the extracted 3D deformation field for comparison. The comparative analysis is presented in Figure 8. In Figure 8, the extracted vertical displacements and horizontal movement along the AB profile align closely with the simulated values, with no significant differences. However, along the CD profile in the south–north direction, there is a slight offset between the extracted and simulated deformation curves, despite similar maximum values and overall shapes.

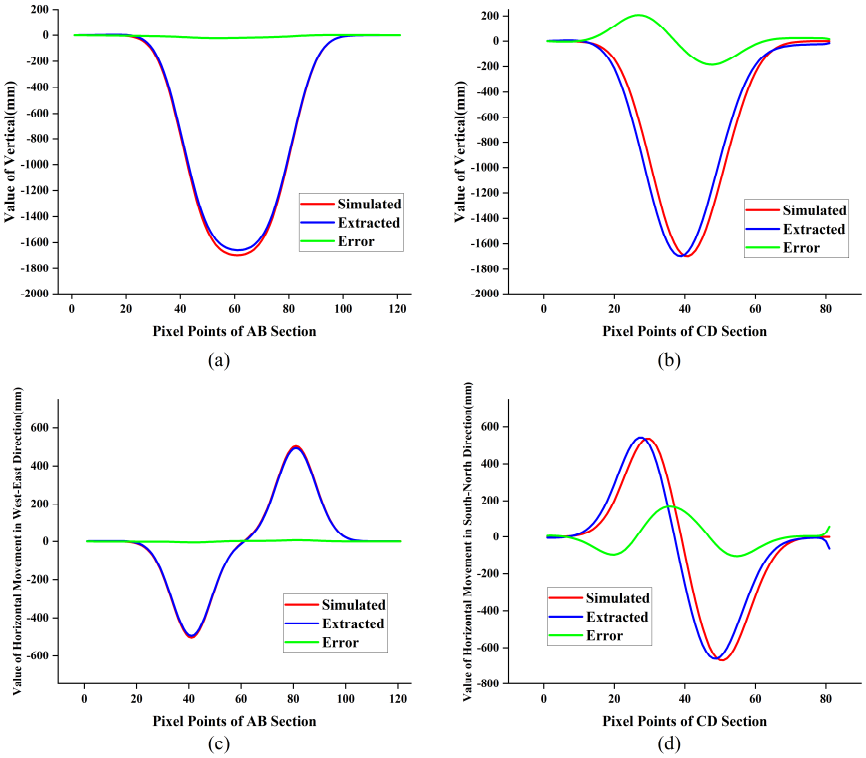


Figure 8. Comparison of 3D deformation values of profile lines extracted based on DLB-3DEM method with simulated values: (**a**) vertical displacements comparison of AB, (**b**) vertical displacements comparison of CD, (**c**) east–west horizontal movement comparison of AB, (**d**) south–north horizontal movement comparison of CD.

The accuracy of the extracted deformation value is evaluated using two indices: root-mean-squared error (RMSE) and relative root mean square error (RRMSE). Results for RMSE and RRMSE, calculated according to Equations (22) and (23), respectively, are summarized in Table 2.

$$\sigma = \sqrt{\frac{\sum_{i=1}^{n} V_i^2}{n}} \tag{22}$$

$$\sigma_r = \frac{\sigma}{v_m} \times 100\% \tag{23}$$

where σ is the RMSE; σ_r is the RRMSE; V represents the difference between the real value and the extracted value; n is the number of points; v_m is the maximum surface displacement value.

Table 2. Deformation extraction accuracy.

Direction	RMSE/mm	RRMSE
Vertical Direction of AB	21.11	1.24%
Vertical Direction of CD	102.72	6.05%
East–west direction of AB	4.88	0.97%
South–north direction of CD	76.85	11.47%

As indicated in Table 2, the RRMSEs of the extracted vertical displacements are less than 10%, and the RRMSEs of the extracted horizontal movements are less than 20%. Therefore, the DLB-3DEM method proposed in this paper is considered feasible.

4. Real Data Experiment

4.1. Study Area and SAR Datasets

The Yuzhou coal mine in Henan Province, China, was selected as the validation site for the proposed DLB-3DEM method. The 2051 working face, roughly oriented east–west, is shown in Figure 9. The mining operation started in October 2020 and ended in February 2022, extracting one coal seam on average each month along the strike direction. A total of 17 coal seam areas were mined, resulting in a final strike length of 664 m and a dip length of 224 m. The mining method used is single horizontal uphill and downhill development, backward fully mechanized mining, large-height longwall mining process in strike direction, and full caving method to manage the roof. The dip azimuth is 172.32° (see Figure 9). The average mining depth was 580 m, and the coal seam dip angle was 6°. The extracted coal seam had an average thickness of 5.0 m. The PIM prediction parameters are as follows: horizontal displacement factor b = 0.3, tangent of main influence angle tan β = 2.3, and angle of maximum subsidence θ = 87°.

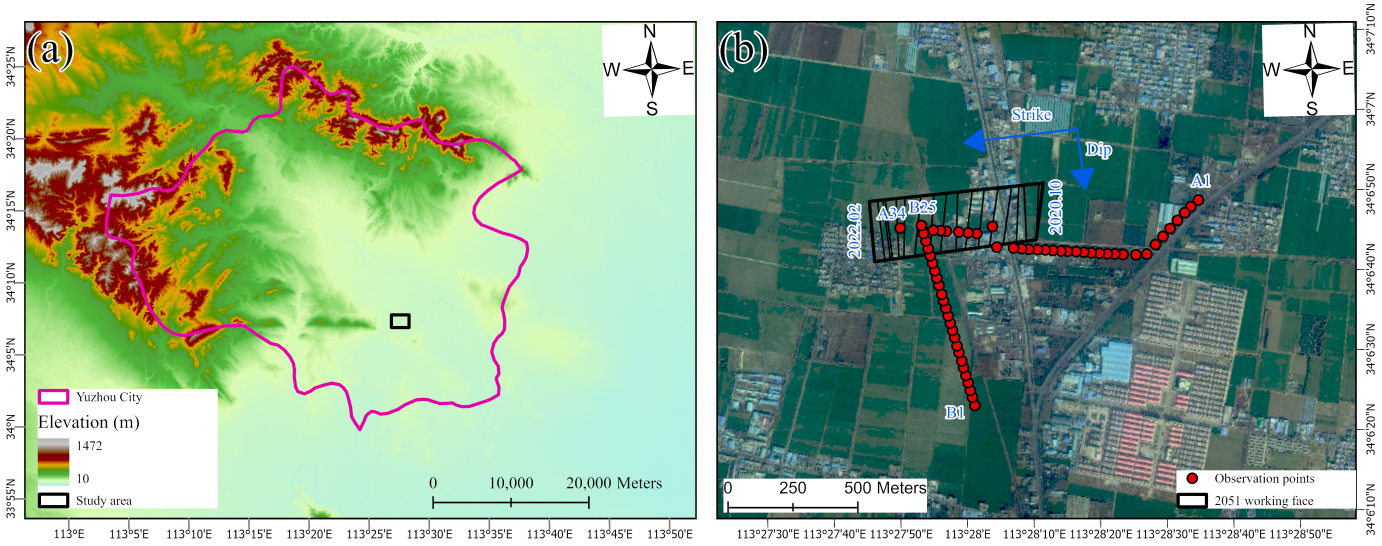


Figure 9. Study area: (**a**) ALOS PALSAR DEM of study area; (**b**) enlarged view of the 2051 working face. The "2020.10" and "2022.02" represent October 2020 and February 2022, respectively, indicating the mining time for the first and last sections of 2051 working face.

A surface movement observation station was established above the 2051 working face. Due to the presence of a large number of buildings and farmland on the surface, the deployment of the surface movement observation station was restricted and could not be set up in the major sections of the subsidence basin. The observation line in dip direction was set up in the form of a straight line along the railroad with a total of 25 measurement points (B1–B25), and the observation line in strike was set up in the form of a broken line along the trail with a total of 34 measurement points (A1–A34). Both lines deviated from the major section of the subsidence basin but passed through the maximum subsidence area. The relative positions of the 2051 working face and the survey lines are shown in Figure 9b. Leveling and GNSS RTK measurements were carried out to determine the 3D coordinates of the observation points from November 2020 to February 2023. The accuracy of the measurement results is reliable and can provide a basis for analyzing the surface movement law in the underground mining area.

SAR data from ESA's Sentinel-1A satellite, with a 12-day revisit period, were utilized for the experiment. The available Sentinel-1A data for the study area are limited to the ascending orbit, which covers the entire region of interest. According to the leveling data from the surface movement observation station, when all the coal seams of the working face were extracted, the final surface subsidence value reached −2 m. In cases of large deformation gradients, traditional D-InSAR technology is inadequate for monitoring [42].

However, at the beginning of the surface subsidence induced by coal seam extraction, the small rate of subsidence allows for effective monitoring using D-InSAR technology [43]. A total of 7 Sentinel-1A SAR images (see Table 3) were selected to analyze the LOS deformation above the 2051 working face from 22 November 2020 to 2 February 2021, during the early stage of surface subsidence. The polarization mode of the Sentinel-1A images is VV polarization.

Table 3. Sentinel-1A dataset and interferometric schemes.

Master Image	Slave Image	Temporal Baseline (Day)	Perpendicular Baseline (m)	Incidence Angle of Master Image (°)	Azimuth (°)
22 November 2020	4 December 2020	12	47	42.0198	347.0167
4 December 2020	16 December 2020	12	3	42.0168	347.0180
16 December 2020	28 December 2020	12	62	42.0166	347.0186
28 December 2020	9 January 2021	12	5	42.0198	347.0167
9 January 2021	21 January 2021	12	−16	42.0127	347.0178
21 January 2021	2 February 2021	12	−99	42.0133	347.0173

4.2. D-InSAR Processing

For the selected SAR data, "two-pass" D-InSAR processing was performed on each image pair [44]. The resulting differential interferometric results from each processing step were then summed to obtain the cumulative LOS deformation over the monitoring period. As shown in Table 3, six interferometric pairs were generated from seven SAR images. In the D-InSAR processing, precise orbit data were utilized to remove errors caused by satellite orbit. The 12.5 m resolution ALOS PALSAR DEM were employed to remove the topographic phases of the interferograms. To enhance the clarity of interference fringes and reduce the decoherence noise, the Goldstein method was applied to filter the interferogram. The Minimum Cost Flow Method was used for phase unwrapping, where the unwrapping process operated only on the pixels with coherence greater than 0.3, and the rest of the pixels will be set to missing values. The resulting LOS deformation maps were geocoded and transformed to the UTM coordinate system based on the WGS84 reference ellipsoid, with a spatial resolution of 15 m in both the east–west and south–north directions.

To extract the 3D deformation field from the LOS deformation field using DLB-3DEM method, the continuity of the LOS deformation field needs to be ensured. The coherence of the study area is illustrated in Figure 10a. As depicted in Figure 10a, there are regions exhibiting decoherence. Therefore, the Kriging interpolation was used to fill in the missing data in LOS deformation fields from coherence lower than 0.3 [45]. The LOS deformation field during the monitoring period is depicted in Figure 10b, reaching a maximum absolute value of approximately 83 mm. As shown in Figure 10b, underground mining in the 2051 working face has resulted in the formation of a LOS deformation field resembling a subsidence basin on the surface. However, a certain degree of deformation is also observed in the LOS deformation field to the southeast of the mining face, away from the working face. This may be due to the influence of topographic errors on deformation measurements during D-InSAR data processing. Due to various surface changes, the DEM data used in the D-InSAR processing may differ from the actual terrain, leading to topographic errors. Particularly in the southeastern part of the study area, where there are numerous residential buildings (see Figure 9b), the changes in these buildings could be a factor contributing to the topographic errors. The impact of topographic errors on interferometric results is still a subject of debate regarding whether it is systematic or random. However, existing studies suggest that in the "two-pass" D-InSAR processing, the deformation errors introduced by topographic data are mainly systematic errors [46]. Therefore, after D-InSAR data processing, it is crucial to focus on the inspection and analysis of deformation results, such as comparing them with measurements from surface movement observation stations.

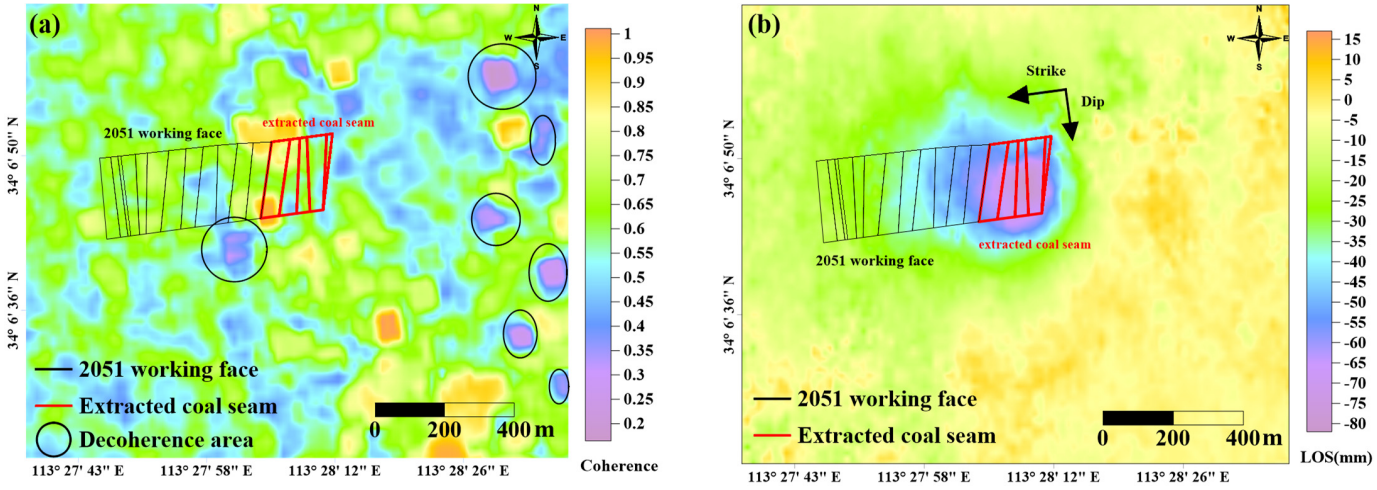


Figure 10. Coherence and LOS deformation field of study area. (**a**) Interferometric coherence; (**b**) LOS deformation field above the working face from 22 November 2020 to 2 February 2021. The area surrounded by black circles represents the decoherence area. The red part of the working face represents the coal seam that has been extracted as of 2 February 2021.

4.3. Real Data Experiment Results and Analysis

Using the DLB-3DEM method, the 3D deformation field above the 2051 working face was extracted from the LOS deformation field, and the uncertainty of the 3D deformation field was estimated. The results of the extraction and uncertainty estimation are depicted in Figure 11. In Figure 11a, the maximum absolute subsidence value extracted is 86 mm, occurring in the right half of the working face, which is due to the left part not being mined in the early stage. In Figure 11b, the maximum absolute horizontal movement in the south–north direction is 51 mm, with larger movements in the southern part of the working face, attributed to the inclination angle of coal seam, consistent with the deformation characteristics of inclined seams. In Figure 11c, the maximum absolute horizontal movement in the east–west direction is 45 mm, with smaller movements on the left side of the working face. Figure 11d shows the maximum standard deviation of subsidence reaching approximately 2.7 mm, with a trend of gradual increase from the northwest to the southeast corner. Figure 11e displays the maximum standard deviation of south–north horizontal movement reaching approximately 382.6 mm, increasing from north to south. Figure 11f shows the maximum standard deviation of east–west horizontal movement reaching approximately 51.4 mm, gradually increasing from east to west. By analyzing the extracted 3D deformation, the extracted 3D deformation above the working face is consistent with the mining-subsidence law.

To quantitatively verify the accuracy of the extracted deformation values, we compared the extracted deformation values with the deformation measurements from 59 monitoring points (A1–A34, B1–B25) at the surface movement observation station. The comparison results are presented in Figure 12. It can be seen that the extracted 3D deformation curves closely follow the trend in the measured deformation curves. The RMSE for subsidence is 14.06 mm, for horizontal movement in the south–north direction is 7.37 mm, and for horizontal movement in the east–west direction is 11.56 mm. In Figure 12a, the surface subsidence extracted from the LOS deformation field was compared with leveling data. For the strike observation line (A1–A34), the extracted subsidence values and the leveling data largely corresponded in the subsidence basin edge area (A1–A16). For the dip observation line (B1–B25), the extracted subsidence values and the leveling data in the subsidence basin edge area (B1–B12) showed a consistent trend but exhibited value discrepancies, characterized as a systematic error. This region (B1–B12) was located in the southeastern part of the LOS deformation field, suggesting that the LOS deformation in this area was likely influenced by systematic errors in the topographic errors.

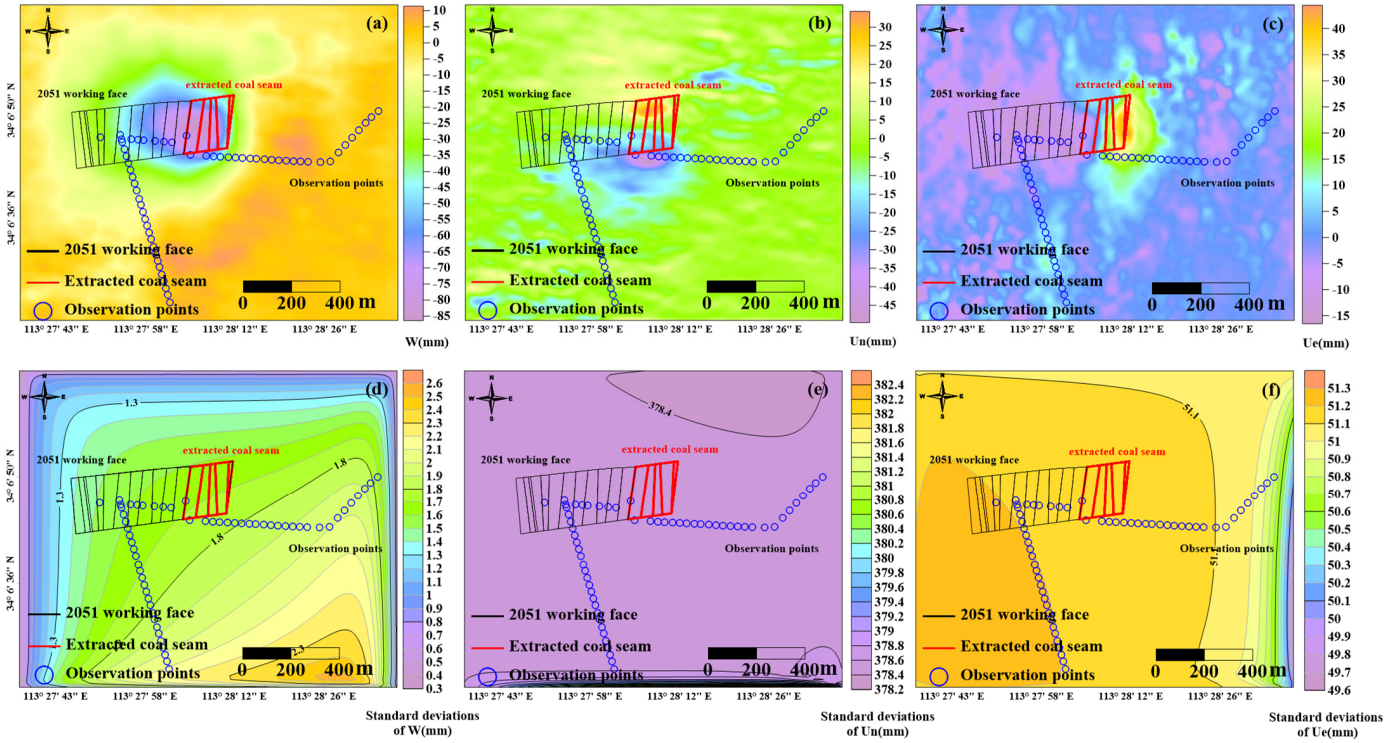


Figure 11. Extracted 3D deformation field and uncertainty evaluation of 2051 working face as of 2 February 2021: (**a**) extracted vertical displacement value, (**b**) extracted south–north horizontal displacement value, (**c**) extracted east–west horizontal displacement value, (**d**) standard deviation map of vertical displacements, (**e**) standard deviation map of south–north horizontal displacements, (**f**) standard deviation map of east–west horizontal displacements.

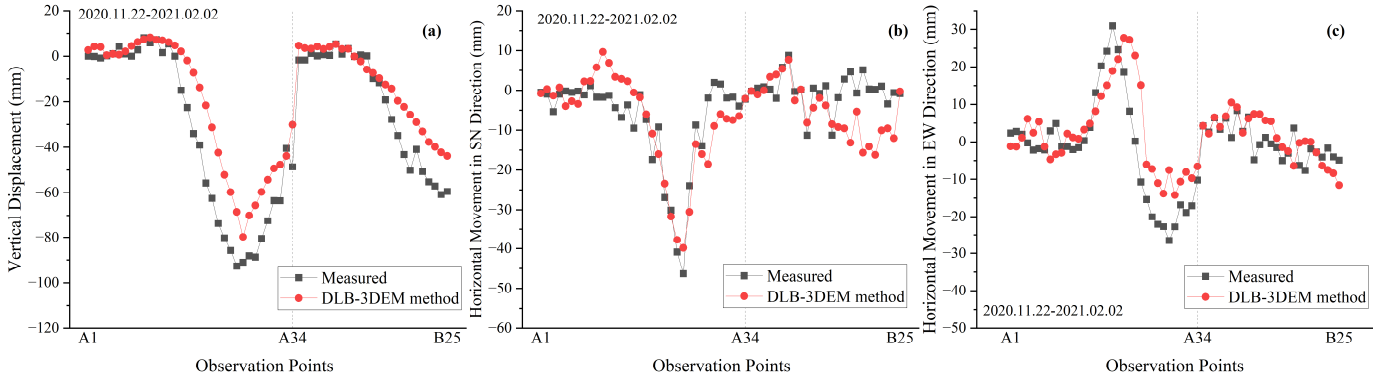


Figure 12. Comparison between measured deformation values and deformation values extracted by the DLB-3DEM method at 59 monitoring points: (**a**) vertical displacement, (**b**) south–north horizontal movement, (**c**) east–west horizontal movement. The meaning of the abscissa observation points indicates that the comparison of the measured and extracted deformation values at the 59 points is conducted in the order of strike direction points (A1–A34) followed by dip direction points (B1–B25).

The differences between the extracted and measured 3D deformations can be attributed to several factors: (1) the LOS deformation obtained by the InSAR technique contains errors, leading to a deformation field that may not fully satisfy the differentiability condition; (2) measurement errors in the deformation values; (3) limitations of the PIM deformation model in accurately representing the actual deformation, i.e., model errors.

The DLB-3DEM method proposed in this paper can provide a certain reference for 3D deformation monitoring in underground mining areas.

5. Discussion

5.1. Influence of LOS Measurement Errors on the DLB-3DEM Method

In Section 3, the simulated LOS deformation field is error-free to validate the feasibility of the proposed DLB-3DEM method. However, in practical scenarios, errors are unavoidable in any measurement, including InSAR measurements. The primary sources of InSAR errors include interferometric phases, baseline parameters, and topographic datasets. To study the impact of InSAR measurement errors, we introduced Gaussian noise into the LOS deformation field simulated in Section 3.1. To assess how the accuracy of the extracted 3D deformation changes with increasing InSAR measurement error, we incorporated Gaussian noise with the mean of 0 cm and standard deviations ranging from 0 cm to 10 cm at 2 cm intervals. Subsequently, the 3D deformation was extracted using the DLB-3DEM method from the LOS deformation field with the added noise. The aforementioned noise errors are illustrated in Figure 13.

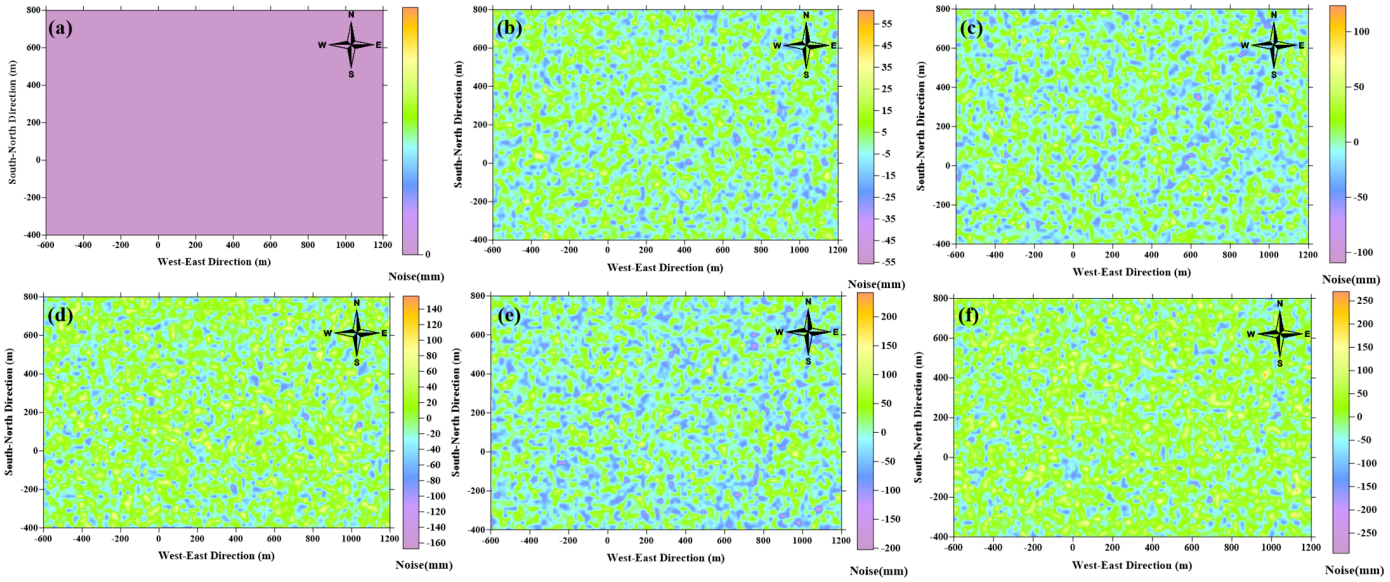


Figure 13. Gaussian noise added to the simulated LOS deformation field: (**a**) no noise; (**b**) mean: 0 mm, standard deviation: 20 mm; (**c**) mean: 0 mm, standard deviation: 40 mm; (**d**) mean: 0 mm, standard deviation: 60 mm; (**e**) mean: 0 mm, standard deviation: 80 mm; (**f**) mean: 0 mm, standard deviation: 100 mm.

For the extracted 3D deformation field, we obtained pixel values along the two profile lines AB and CD mentioned in Section 3.2 and compared them with the simulated true values. The comparison results for subsidence and horizontal movement are presented in Figures 14 and 15, respectively. The extraction accuracy of the profile lines is detailed in Table 4.

Figures 14 and 15 illustrate that as the added error increases, the extraction error gradually rises, and the smoothness of the extracted deformation curves diminishes. Notably, the smoothness of the horizontal movement curves diminishes faster than that of the subsidence curves. This phenomenon arises from the fact that, in the DLB-3DEM method, horizontal movement is proportional to the subsidence gradient. When the smoothness of the subsidence curve diminishes, the smoothness of the horizontal movement curve is affected more significantly. Therefore, InSAR measurement errors have a greater impact on the accuracy of extracting horizontal movement. However, the size and shape of the extracted deformation curves remain similar to the real values, demonstrating that the DLB-3DEM method can still effectively extract 3D deformations.

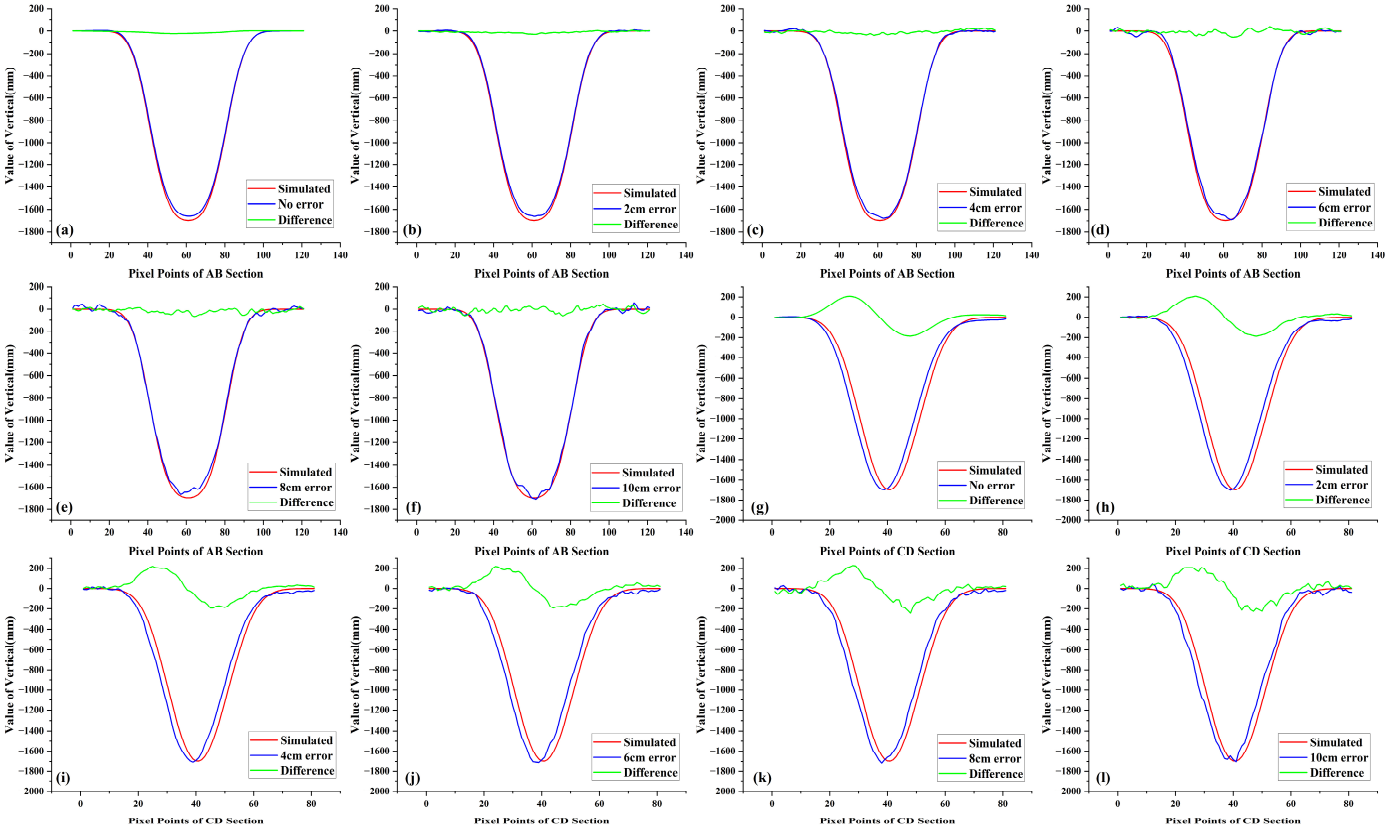


Figure 14. Comparison of subsidence extracted and the real values as the error increases. The red curve represents the true value, the blue curve represents the extracted value after adding the specified error, and the green curve represents the difference between the two. (**a**–**f**) Subsidence comparison of AB, (**g**–**l**) subsidence comparison of CD.

From Table 4, it can be seen that the RMSE, RRMSE, and error range of the extracted deformation values gradually increase with the increase in the added error, but the increase in the error of subsidence is smaller than that of the horizontal movement, which is consistent with the previous conclusion. However, the RRMSE of subsidence is not greater than 10%, and the RRMSE of horizontal movement is not greater than 20%, which can meet the accuracy requirements. Although the error gradually increases, the size of the error is much smaller than the size of the 3D deformation, which is in the acceptable accuracy range. The error of horizontal movement is greater than that of subsidence, because horizontal movement is calculated using subsidence, and the error is amplified during calculation. In summary, it can be proved that the DLB-3DEM method can still be able to effectively extract the 3D deformation in the presence of large InSAR measurement errors.

Table 4. Change in accuracy as error increases.

Direction	Added Error/mm	RMSE/mm	RRMSE	Error Range/mm
Vertical Direction of AB	0	21.11	1.24%	−40.72~0.58
	20	21.07	1.24%	−42.95~7.876
	40	20.95	1.23%	−47.53~10.78
	60	27.24	1.60%	−62.35~48.85
	80	29.91	1.76%	−84.42~45.93
	100	23.32	1.37%	−69.11~38.06

Table 4. *Cont.*

Direction	Added Error/mm	RMSE/mm	RRMSE	Error Range/mm
Vertical Direction of CD	0	102.72	6.05%	−185.22~206.55
	20	102.57	6.04%	−185.52~205.48
	40	104.15	6.14%	−183.44~206.13
	60	109.08	6.43%	−215.29~214.88
	80	102.80	6.06%	−189.15~234.33
	100	101.69	5.99%	−192.09~244.56
EW direction of AB	0	4.88	0.97%	−8.99~9.74
	20	11.91	2.36%	−27.00~31.59
	40	22.08	4.38%	−62.75~48.54
	60	38.34	7.61%	−77.82~98.60
	80	50.63	10.05%	−121.66~103.29
	100	60.13	11.93%	−174.05~138.11
NS direction of CD	0	76.85	11.47%	−104.92~170.07
	20	77.90	11.63%	−139.88~191.37
	40	86.40	12.90%	−170.63~228.16
	60	98.86	14.76%	−207.36~265.78
	80	104.46	15.60%	−236.08~307.00
	100	119.15	17.79%	−282.15~306.61

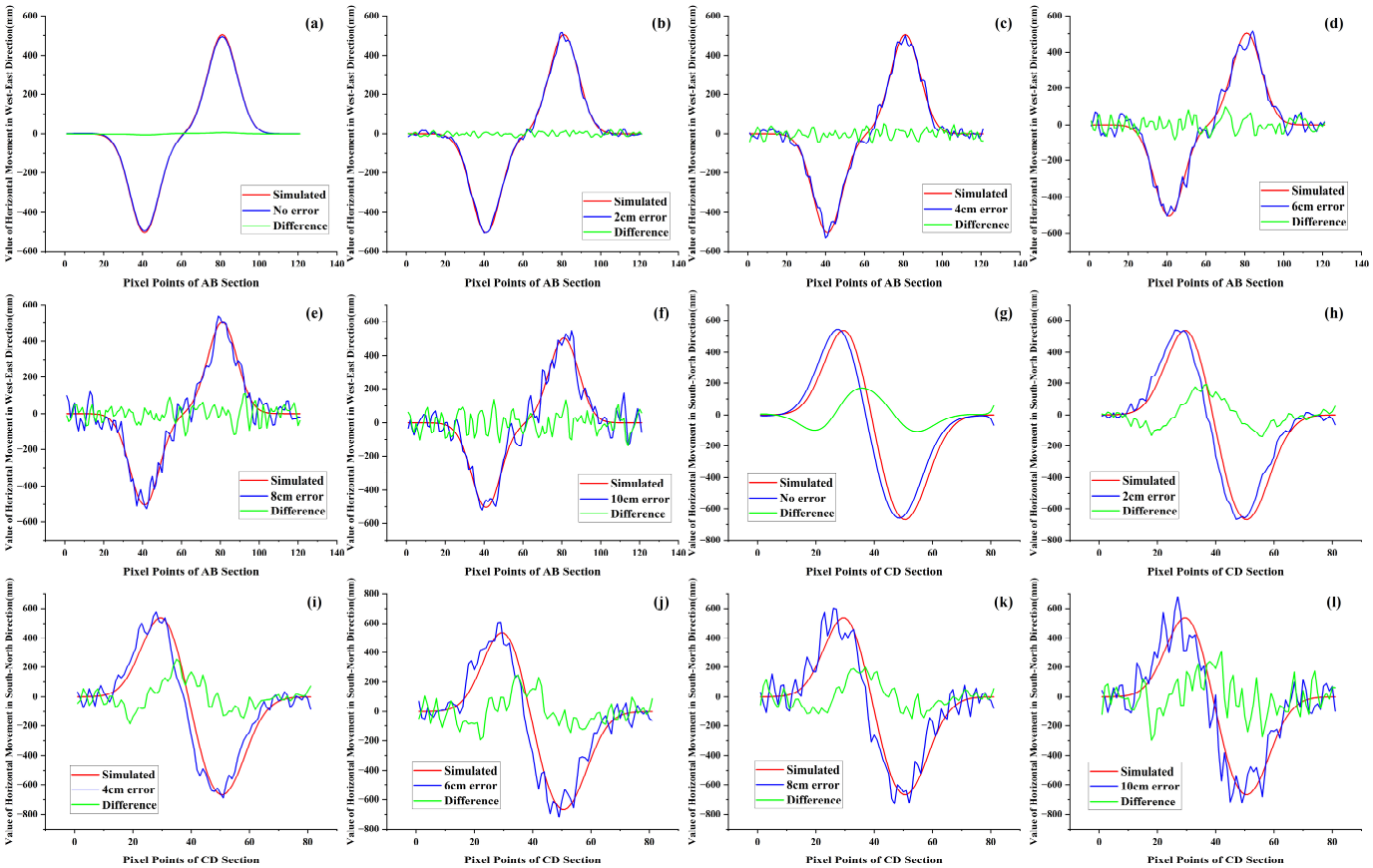


Figure 15. Comparison of horizontal movement extracted and the real values as the error increases. The red curve represents the true value, the blue curve represents the extracted value after adding the specified error, and the green curve represents the difference between the two. (**a**–**f**) Horizontal movement comparison of AB, (**g**–**l**) horizontal movement comparison of CD.

5.2. Influence of PIM Parameter Errors on the DLB-3DEM Method

The DLB-3DEM method requires PIM prediction parameters in the study area, including horizontal displacement factor b, tangent of main influence angle $\tan\beta$, angle of maximum subsidence θ. The methods of obtaining the above parameters can be divided into two: (1) determining the empirical values of the PIM parameters according to the geological mining conditions and (2) inverting the PIM parameters based on the actual measured data. However, no matter which method, the acquired PIM parameters inevitably have errors. In this Section, we will discuss the effect of the parameter error of PIM on the DLB-3DEM method based on the simulated experimental conditions in Section 3.1.

As the coal seam dip angle α increases, the value of maximum subsidence angle θ decreases. Its calculation formula can be obtained from the measured data of the mining area in China as shown in Equation (24) [38,39]. However, when $\alpha > 60^\circ \sim 70^\circ$, the maximum subsidence angle θ no longer decreases with the increase of α but increases with the increase of α, although not greater than 90°. For clarity in our discussion, we convert the discussion of angle of maximum subsidence θ to a discussion of coefficient k in Equation (24).

$$\theta = 90^\circ - k \cdot \alpha \tag{24}$$

where α is the coal seam dip angle; k is the coefficient, related to lithology, with different values for different mining areas.

First, the LOS deformation field without error in Section 3.1 was selected. Subsequently, errors ranging from -50% to 50% were added at 10% intervals for b, $\tan\beta$, and k, respectively. The method examines the impact of individual parameter errors on the model while keeping the other two parameters error-free. Employing this approach, we obtained 30 sets of parameters, with 10 sets for each parameter. Subsequently, the 3D deformation was extracted using the DLB-3DEM method. Finally, we analyzed the accuracy of deformation extraction along the two profile lines AB and CD as outlined in Section 3.2.

Figure 16 illustrates the relative-errors trend in 3D deformations extracted from profile lines AB and CD as influenced by errors in the three PIM parameters. It is evident that deformation extraction errors increase gradually with the magnitude of parameter errors. To compare the impact of these parameter errors on extraction accuracy, we computed the average relative error of deformation extraction results under different parameter error conditions. As depicted in Figure 17, the accuracy of subsidence extraction is significantly better than that of horizontal movement. Among the three parameters, the $\tan\beta$ exhibits the most substantial influence on deformation accuracy, followed by the b, with k having the least impact. However, the average relative error remains below 10% for subsidence and 20% for horizontal movement. This suggests that the effect of PIM parameter errors on deformation extraction accuracy is within acceptable limits.

5.3. Ill-Posed Problem of DLB-3DEM Method

During the construction of the DLB-3DEM method in Section 2.2, we made the assumption that the observations L in Equation (16) were independent of each other. However, in reality, the observations L are correlated, being a function of the direct observation LOS deformation field. Consequently, solving Equation (16) becomes a problem of adjustment of correlated observations.

The InSAR measurements are related to the coherence, the greater the coherence, the more accurate the measurements, where the value of the coherence is between 0 and 1. As mentioned earlier, we assume that the coherence coefficient map of InSAR is C after expanding it in the order of rows. Let the cofactor matrix of the direct observation LOS be $\mathrm{diag}(1/C)$, and then according to Equation (13), the cofactor matrix Q of the observation L can be obtained as follows:

$$Q = \begin{pmatrix} D_0 \\ D_{\pi/4} \\ D_{\pi/2} \\ D_{3\pi/4} \\ D_{\pi} \\ D_{5\pi/4} \\ D_{3\pi/2} \\ D_{7\pi/4} \end{pmatrix} \mathrm{diag}(1/C) \begin{pmatrix} D_0 \\ D_{\pi/4} \\ D_{\pi/2} \\ D_{3\pi/4} \\ D_{\pi} \\ D_{5\pi/4} \\ D_{3\pi/2} \\ D_{7\pi/4} \end{pmatrix}^T \tag{25}$$

where $\mathrm{diag}(1/C)$ is a diagonal matrix with vector $1/C$ as the diagonal element.

The weight matrix of the observation L is $P = Q^{-1}$. The solution to Equation (16) is then the following:

$$W = \left(B^T P B\right)^{-1} B^T P L \tag{26}$$

It is more reasonable to consider the correlation of the observation L by expressing it in terms of the direct observation LOS. However, in this scenario, the presence of numerous unknown parameters inevitably leads to an approximate linear relationship among them. This approximation induces linear correlation among the column vectors of the coefficient matrices, rendering the matrices close to singular and pathological. Consequently, the Equations become ill-conditioned, posing a challenge to their solution. How to take the coherence of InSAR into account in the model constructed in this paper and to extract reliable deformations from the ill-posed problem are further problems to be solved.

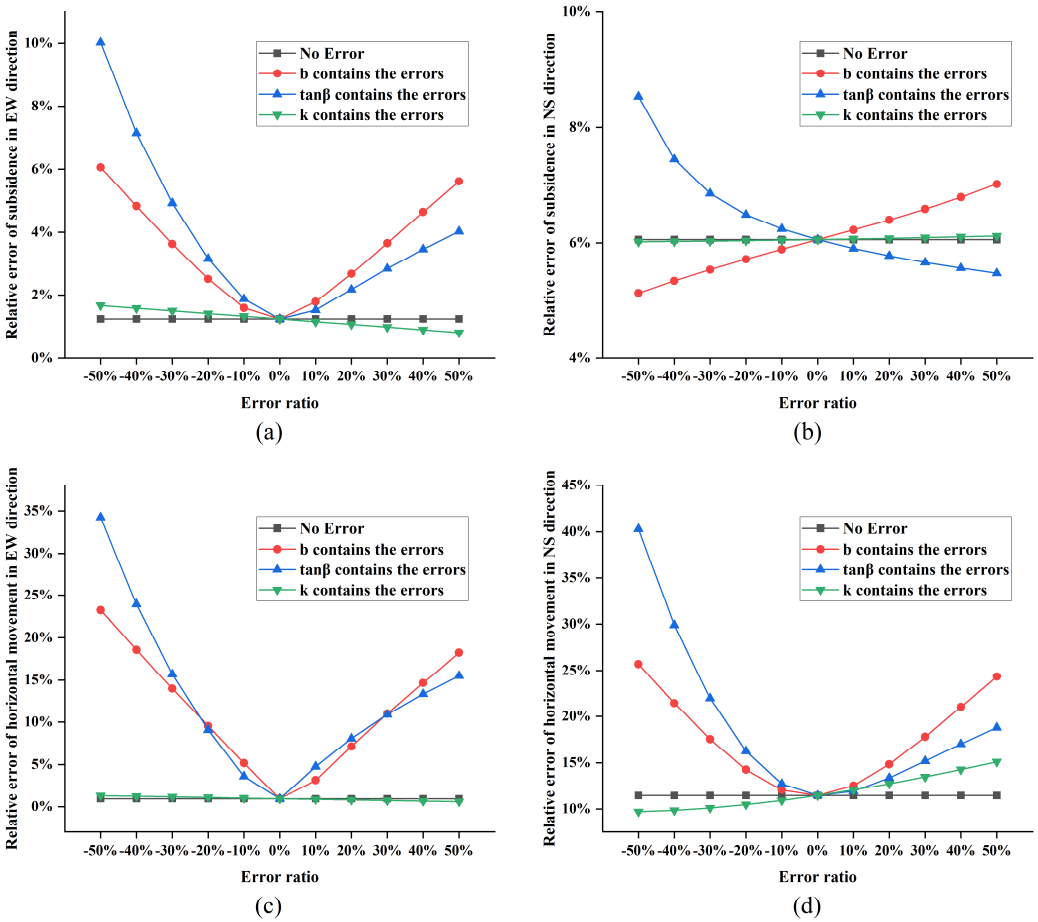


Figure 16. Relative error of 3D deformation extraction results. (**a**) Subsidence of AB, (**b**) subsidence of CD, (**c**) horizontal movement of AB, (**d**) horizontal movement of CD.

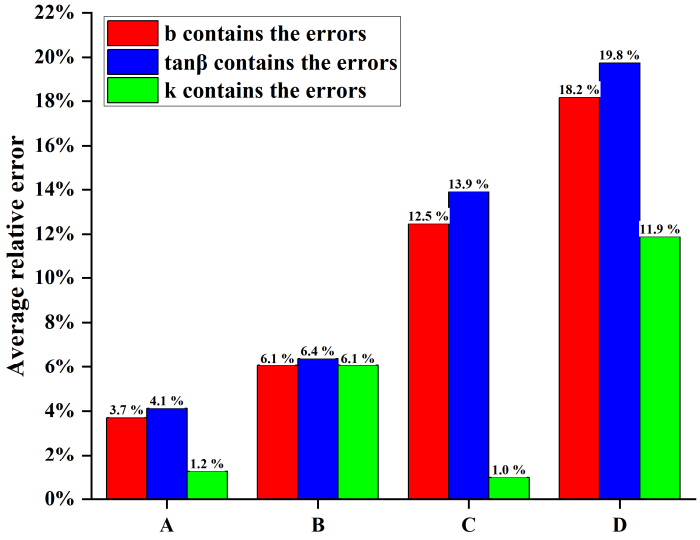


Figure 17. Average relative error of 3D deformation. (A) Subsidence of AB, (B) subsidence of CD, (C) horizontal movement of AB, (D) horizontal movement of CD.

6. Conclusions

(1) Proposed method: This paper proposes a new method (DLB-3DEM method) for extracting 3D surface deformation in underground mining areas based on the differentiability of the D-InSAR LOS deformation field. The method uses the existence of directional derivatives of the differentiable function to construct a 3D deformation extraction model. Using the least squares method, the model estimates the 3D deformation and evaluates its uncertainty. The DLB-3DEM method can extract 3D surface deformation for both horizontal and inclined coal seams.

(2) Simulation and real data validation: Simulation experiments and real data experiments were used to verify the feasibility of the DLB-3DEM method. Simulation experiments show that the RRMSEs of subsidence and horizontal displacement in east–west and south–north directions are 1.24%, 6.05%, 0.97%, and 11.47%, respectively. The accuracy of subsidence is higher than that of horizontal displacement because in the DLB-3DEM method, subsidence is directly solved by the equation, and horizontal displacement is further calculated from subsidence, which increases the error in the calculation process. The deformation extraction accuracy in the east–west direction is higher than that in the south–north direction, which is related to the dip direction of the coal seam, which affects the deformation extraction accuracy of the model in different directions. Real data experiments use 7 Sentinel-1 images to extract 3D surface deformation above the 2051 working face between 22 November 2020 and 2 February 2021 in the Yuzhou coal mine area. Comparing the extracted values with the field measured values, the RMSEs in the up–down, south–north, and east–west directions are 14.06 mm, 7.37 mm, and 11.56 mm, respectively. The results of the simulation and real data experiments show that this method is able to efficiently extract the mining-induced 3D surface deformation.

(3) Error analysis and future research: The influence of InSAR measurement errors and PIM parameter errors on the DLB-3DEM method are discussed, and the results show that the influence of the two errors on the deformation extraction accuracy are acceptable. It is analyzed that the deformation extraction model is an ill-posed problem when considering InSAR coherence, and how to solve this problem is worth considering.

Author Contributions: Conceptualization, J.C.; resources, J.C. and W.Y.; funding acquisition, J.C. and W.Y.; methodology, C.Z.; software, C.Z.; writing—original draft, C.Z.; writing—review and editing, W.Y.; visualization, Z.C. All authors have read and agreed to the published version of the manuscript.

Funding: This research was funded by the National Natural Science Foundation of China: (42207534, U21A20108, 52274165); Natural Science Foundation of Henan Province: (242300421363); Excellent Youth Foundation of Henan Polytechnic University: (J2024-4); Training Plan for Young Backbone Teachers in Higher Education Institutions in Henan Province (2024GGJS038).

Data Availability Statement: The Sentinel-1 data of this study are available in ESA/Copernicus at https://scihub.copernicus.eu, accessed on 1 March 2024. The ALOS PALSAR data were provided through the Alaska Satellite Facility.

Acknowledgments: The authors gratefully acknowledge the Sentinel-1 data provided by ESA/Copernicus, and the ALOS PALSAR data provided by the Alaska Satellite Facility.

Conflicts of Interest: The authors declare no conflicts of interest.

References

1. Zhang, Y.; He, K.; Hu, X.; Liu, W.; Zhang, S.; Wu, J.; Xi, C. Mechanism of surface subsidence and sinkhole formation in mining areas: Insights from MPM. *Bull. Eng. Geol. Environ.* **2024**, *83*, 330. [CrossRef]
2. Suh, J.; Choi, Y. Mapping hazardous mining-induced sinkhole subsidence using unmanned aerial vehicle (drone) photogrammetry. *Environ. Earth Sci.* **2017**, *76*, 144. [CrossRef]
3. Gayarre, F.L.; Álvarez-Fernández, M.I.; González-Nicieza, C.; Álvarez-Vigil, A.E.; García, G.H. Forensic analysis of buildings affected by mining subsidence. *Eng. Fail. Anal.* **2010**, *17*, 270–285. [CrossRef]
4. Liu, Z.; Cui, B.; Liang, Y.; Guo, H.; Li, Y. Study on foundation deformation of buildings in mining subsidence area and surface subsidence prediction. *Geotech. Geol. Eng.* **2019**, *37*, 1755–1764. [CrossRef]
5. Bi, Y.; Zhang, J.; Song, Z.; Wang, Z.; Qiu, L.; Hu, J.; Gong, Y. Arbuscular mycorrhizal fungi alleviate root damage stress induced by simulated coal mining subsidence ground fissures. *Sci. Total Environ.* **2019**, *652*, 398–405. [CrossRef]
6. Liu, H.; Deng, K.; Zhu, X.; Jiang, C. Effects of mining speed on the developmental features of mining-induced ground fissures. *Bull. Eng. Geol. Environ.* **2019**, *78*, 6297–6309. [CrossRef]
7. Tong, L.; Leo, L.; Amatya, B.; Liu, S. Risk assessment and remediation strategies for highway construction in abandoned coal mine region: Lessons learned from Xuzhou, China. *Bull. Eng. Geol. Environ.* **2016**, *75*, 1045–1066. [CrossRef]
8. Hu, Z.; Hu, F.; Li, J.; Li, H. Impact of coal mining subsidence on farmland in eastern China. *Int. J. Surf. Min. Reclam. Environ.* **1997**, *11*, 91–94. [CrossRef]
9. Gao, J.-X.; Hu, H. Advanced GNSS technology of mining deformation monitoring. *Procedia Earth Planet. Sci.* **2009**, *1*, 1081–1088. [CrossRef]
10. Ignjatović Stupar, D.; Rošer, J.; Vulić, M. Investigation of unmanned aerial vehicles-based photogrammetry for large mine subsidence monitoring. *Minerals* **2020**, *10*, 196. [CrossRef]
11. Zhang, Y.; Lian, X.; Ge, L.; Liu, X.; Du, Z.; Yang, W.; Wu, Y.; Hu, H.; Cai, Y. Surface subsidence monitoring induced by underground coal mining by combining DInSAR and UAV photogrammetry. *Remote Sens.* **2022**, *14*, 4711. [CrossRef]
12. Zheng, J.; Yao, W.; Lin, X.; Ma, B.; Bai, L. An accurate digital subsidence model for deformation detection of coal mining areas using a UAV-based LiDAR. *Remote Sens.* **2022**, *14*, 421. [CrossRef]
13. Liu, X.; Zhu, W.; Lian, X.; Xu, X. Monitoring mining surface subsidence with multi-temporal three-dimensional unmanned aerial vehicle point cloud. *Remote Sens.* **2023**, *15*, 374. [CrossRef]
14. Gu, Y.; Zhou, D.; Zhang, D.; Wu, K.; Zhou, B. Study on subsidence monitoring technology using terrestrial 3D laser scanning without a target in a mining area: An example of Wangjiata coal mine, China. *Bull. Eng. Geol. Environ.* **2020**, *79*, 3575–3583. [CrossRef]
15. Zhou, D.; Wu, K.; Chen, R.; Li, L. GPS/terrestrial 3D laser scanner combined monitoring technology for coal mining subsidence: A case study of a coal mining area in Hebei, China. *Nat. Hazards* **2014**, *70*, 1197–1208. [CrossRef]
16. Yang, Z.; Li, Z.; Zhu, J.; Wang, Y.; Wu, L. Use of SAR/InSAR in mining deformation monitoring, parameter inversion, and forward predictions: A review. *IEEE Geosci. Remote Sens. Mag.* **2020**, *8*, 71–90. [CrossRef]
17. Rauhala, A.; Tuomela, A.; Davids, C.; Rossi, P.M. UAV remote sensing surveillance of a mine tailings impoundment in sub-arctic conditions. *Remote Sens.* **2017**, *9*, 1318. [CrossRef]
18. Hooper, A.; Zebker, H.; Segall, P.; Kampes, B. A new method for measuring deformation on volcanoes and other natural terrains using InSAR persistent scatterers. *Geophys. Res. Lett.* **2004**, *31*, 23. [CrossRef]
19. Berardino, P.; Fornaro, G.; Lanari, R.; Sansosti, E. A new algorithm for surface deformation monitoring based on small baseline differential SAR interferograms. *IEEE Trans. Geosci. Remote Sens.* **2002**, *40*, 2375–2383. [CrossRef]
20. Chen, B.; Li, Z.; Yu, C.; Fairbairn, D.; Kang, J.; Hu, J.; Liang, L. Three-dimensional time-varying large surface displacements in coal exploiting areas revealed through integration of SAR pixel offset measurements and mining subsidence model. *Remote Sens. Environ.* **2020**, *240*, 111663. [CrossRef]
21. Zhu, J.; Yang, Z.; Li, Z. Recent progress in retrieving and predicting mining-induced 3D displace-ments using InSAR. *Acta Geod. Cartogr. Sin.* **2019**, *48*, 135–144. [CrossRef]

22. Fan, H.; Wen, B.; Liu, J.; Liu, J.; Yin, J. An improved method of three-dimensional displacement field generation in mining areas with a single InSAR pair. *Eur. J. Remote Sens.* **2019**, *52*, 493–503. [CrossRef]
23. Ng, A.H.-M.; Ge, L.; Zhang, K.; Chang, H.-C.; Li, X.; Rizos, C.; Omura, M. Deformation mapping in three dimensions for underground mining using InSAR–Southern highland coalfield in New South Wales, Australia. *Int. J. Remote Sens.* **2011**, *32*, 7227–7256. [CrossRef]
24. Samsonov, S.; d'Oreye, N.; Smets, B. Ground deformation associated with post-mining activity at the French–German border revealed by novel InSAR time series method. *Int. J. Appl. Earth Obs. Geoinf.* **2013**, *23*, 142–154. [CrossRef]
25. He, L.; Wu, L.; Liu, S.; Wang, Z.; Su, C.; Liu, S.-N. Mapping two-dimensional deformation field time-series of large slope by coupling DInSAR-SBAS with MAI-SBAS. *Remote Sens.* **2015**, *7*, 12440–12458. [CrossRef]
26. Wang, Z.; Yu, S.; Tao, Q.; Liu, G.; Hao, H.; Wang, K.; Zhou, C. A method of monitoring three-dimensional ground displacement in mining areas by integrating multiple InSAR methods. *Int. J. Remote Sens.* **2018**, *39*, 1199–1219. [CrossRef]
27. Fan, H.; Cheng, D.; Deng, K.; Chen, B.; Zhu, C. Subsidence monitoring using D-InSAR and probability integral prediction modelling in deep mining areas. *Surv. Rev.* **2015**, *47*, 438–445. [CrossRef]
28. Wang, L.; Li, N.; Zhang, X.-N.; Wei, T.; Chen, Y.-F.; Zha, J.-F. Full parameters inversion model for mining subsidence prediction using simulated annealing based on single line of sight D-InSAR. *Environ. Earth Sci.* **2018**, *77*, 161. [CrossRef]
29. Wang, L.; Zhang, X.; Chi, S.; Zha, J. Parameter inversion model for mining subsidence prediction based on fusion of InSAR and GA. *Geomat. Inf. Sci. Wuhan Univ.* **2018**, *43*, 1635–1641. [CrossRef]
30. Yang, Z.F.; Li, Z.W.; Zhu, J.J.; Hu, J.; Wang, Y.J.; Chen, G.L. InSAR-based model parameter estimation of probability integral method and its application for predicting mining-induced horizontal and vertical displacements. *IEEE Trans. Geosci. Remote Sens.* **2016**, *54*, 4818–4832. [CrossRef]
31. Zhu, C.; Wang, Z.; Li, P.; Motagh, M.; Zhang, L.; Jiang, Z.; Long, S. Retrieval and prediction of three-dimensional displacements by combining the DInSAR and probability integral method in a mining area. *IEEE J. Sel. Top. Appl. Earth Obs. Remote Sens.* **2020**, *13*, 1206–1217. [CrossRef]
32. Li, Z.W.; Yang, Z.F.; Zhu, J.J.; Hu, J.; Wang, Y.J.; Li, P.X.; Chen, G.L. Retrieving three-dimensional displacement fields of mining areas from a single InSAR pair. *J. Geod.* **2015**, *89*, 17–32. [CrossRef]
33. Wang, L.; Jiang, C.; Zhang, X.; Li, N.; Zha, J. Monitoring method of surface subsidence induced by inclined coal seam mining based on single line of sight D-InSAR. *Geomat. Inf. Sci. Wuhan Univ.* **2019**, *44*, 814–820. [CrossRef]
34. Fan, H.; Wang, L.; Wen, B.; Du, S. A new model for three-dimensional deformation extraction with single-track InSAR based on mining subsidence characteristics. *Int. J. Appl. Earth Obs. Geoinf.* **2021**, *94*, 102223. [CrossRef]
35. Jiang, C.; Wang, L.; Yu, X.; Lv, W.; Yang, X. A New Method of Monitoring 3D Mining-Induced Deformation in Mountainous Areas Based on Single-Track InSAR. *KSCE J. Civ. Eng.* **2022**, *26*, 2392–2407. [CrossRef]
36. Zhao, R.; Viktorovich, Z.A.; Li, J.; Chen, C.; Zheng, M. A New Strategy for Extracting 3D Deformation of Mining Areas from a Single-Geometry Synthetic Aperture Radar Dataset. *Remote Sens.* **2023**, *15*, 5244. [CrossRef]
37. Hanssen, R.F. *Radar Interferometry: Data Interpretation and Error Analysis*; Springer Science & Business Media: Berlin/Heidelberg, Germany, 2001; Volume 2. [CrossRef]
38. He, G.; Yang, L.; Ling, G.; Jia, F.; Hong, D. *Coal Mining Subsidence*; China University of Mining & Technology Publisher: Xuzhou, China, 1991.
39. Peng, S. *Surface Subsidence Engineering: Theory and Practice*; Csiro Publishing: Clayton, Australia, 2020.
40. LeVeque, R.J. Finite difference methods for differential equations. *Draft Version Use AMath* **1998**, *585*, 112.
41. Hu, J.; Li, Z.; Ding, X.; Zhu, J.; Sun, Q. Derivation of 3-D coseismic surface displacement fields for the 2011 M w 9.0 Tohoku-Oki earthquake from InSAR and GPS measurements. *Geophys. J. Int.* **2013**, *192*, 573–585. [CrossRef]
42. Li, J.; Yan, Y.; Cai, J. LOS Deformation Correction Method for DInSAR in Mining Areas by Fusing Ground Data without Control Points. *Remote Sens.* **2023**, *15*, 4862. [CrossRef]
43. Wempen, J.M. Application of DInSAR for short period monitoring of initial subsidence due to longwall mining in the mountain west United States. *Int. J. Min. Sci. Technol.* **2020**, *30*, 33–37. [CrossRef]
44. Zhang, K.; Ng, A.H.-M.; Ge, L.; Dong, Y.; Rizos, C. L-band and C-band combined interferometric monitoring of the Wenchuan Earthquake. In *Advances in Earth Observation of Global Change*; Springer: Dordrecht, The Netherlands, 2010; pp. 239–253. [CrossRef]
45. Oliver, M.A.; Webster, R. Kriging: A method of interpolation for geographical information systems. *Int. J. Geogr. Inf. Syst.* **1990**, *4*, 313–332. [CrossRef]
46. Liu, G. Mapping of Earth Deformations with Satellite SAR Interferometry: A Study of Its Accuracy and Reliability Performances. Ph.D. Thesis, Hong Kong Polytechnic University, Hong Kong, China, 2003.

Disclaimer/Publisher's Note: The statements, opinions and data contained in all publications are solely those of the individual author(s) and contributor(s) and not of MDPI and/or the editor(s). MDPI and/or the editor(s) disclaim responsibility for any injury to people or property resulting from any ideas, methods, instructions or products referred to in the content.